Efficient Elimination of Chlorinated Organics on A Phosphoric Acid Modified CeO_2 Catalyst: A Hydrolytic Destruction Route

Xiaoxia Dai[1], Xinwei Wang[2], Yunpeng Long[1], Samuel Pattisson[3], Yunhao Lu[2], David J. Morgan[3], Stuart H. Taylor[3], James H. Carter[3]*, Graham J. Hutchings[3], Zhongbiao Wu[1,4], Xiaole Weng[1,4]*

[1]Key Laboratory of Environment Remediation and Ecological Health, Ministry of Education, College of Environmental and Resource Sciences, Zhejiang University, Hangzhou, P. R. China.

[2]State Key Laboratory of Silicon Materials Department of Materials Science and Engineering, Zhejiang University, Hangzhou, P. R. China.

[3]Cardiff Catalysis Institute, School of Chemistry, Cardiff University, Park Place, Cardiff CF10 3AT, United Kingdom.

[4]Zhejiang Provincial Engineering Research Center of Industrial Boiler & Furnace Flue Gas Pollution Control, 388 Yuhangtang Road, 310058 Hangzhou, P. R. China.

*Corresponding authors. E-mail: xlweng@zju.edu.cn; CarterJ5@cardiff.ac.uk.

Abstract

The development of efficient technologies to prevent the emission of hazardous chlorinated organics from industrial sources without forming harmful by-products, such as dioxins, is a major challenge in environmental chemistry. Herein, we report a new hydrolytic destruction route for efficient chlorinated organics elimination and demonstrate that phosphoric acid modified CeO_2 (HP-CeO_2) can decompose chlorobenzene (CB) without forming polychlorinated congeners under the industry-relevant reaction conditions. The active site and reaction pathway were investigated, and it was found that surface phosphate groups initially react with CB and water to form phenol and HCl, followed by deep oxidation. The high on-stream stability of the catalyst was due to the efficient generation of HCl, which removes Cl from the catalyst surface and ensures O_2 activation and therefore deep oxidation of the hydrocarbons.

Subsequent density functional theory (DFT) calculations revealed a distinctly decreased formation energy of an oxygen vacancy at nearest (V_{O-1}) and next-nearest (V_{O-2}) surface sites to the bonded phosphate groups, which likely contributes to the high rate of oxidation observed over the catalyst. Significantly, no dioxins, which are frequently formed in the conventional oxidation route, were observed. This work not only reports an efficient route and corresponding phosphate active site for chlorinated organics elimination, but also illustrates that rational design of reaction route can solve some of the most important challenges in environmental catalysis.

Keywords: Chlorinated organics, Phosphate, Hydrolysis destruction, CeO_2, Dioxin

TOC/Abstract Art

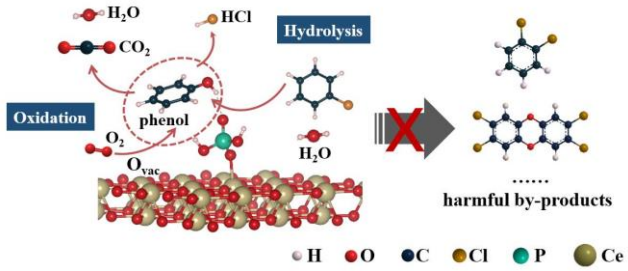

1. INTRODUCTION

Chlorinated organics have widespread industrial applications in the manufacture of polyvinyl chloride, pharmaceuticals, herbicides and fungicides [1, 2]. Certain quantities are also present in the flue gas of municipal solid waste incineration and metal smelting and refining processes [3, 4]. Such chlorinated compounds are listed by the United States Environmental Protection Agency as environmental priority control pollutants due to their inherent bioaccumulation and potential carcinogenicity [5]. Therefore, the destruction of these compounds prior to emission is of the upmost importance. In particular, polychlorinated dibenzofurans, biphenyls and hexachlorobenzenes are classified as Persistent Organic Pollutants (POPs) by the Stockholm Convention. These POPs, together with other polychlorinated congeners, are formed as by-products in combustion processes *via* the condensation of chlorinated hydrocarbons, chlorophenols or chlorobenzenes (CBs) in a series of reactions (e.g. Ullmann reaction [6]) [7]. These condensation reactions occur especially at 250-450 °C [7] on the surface of fly ash [8] and industrial catalysts [9, 10].

The development of stable and selective catalysts for the destruction of chlorinated organics is an active research field of global importance. Commercially viable catalysts must directly oxidize the chlorinated compounds into harmless products without forming polychlorinated side-products. However, the electronegativity of chlorine makes it preferentially adsorb on electrophilic surface sites, e.g. noble metals, oxygen vacancies, Brønsted and Lewis acid sites. This leads to the accumulation of chlorine on the surface and the inhibition of sufficient oxidation. The accumulated chlorine ultimately leads to catalyst chlorination and promotes the formation of harmful polychlorinated by-products, such as dioxins. Condensation reactions can be minimized by operating below 250 °C and so a commercially-viable catalyst should be active in this temperature range.

Previously, U_3O_8 [11] and VO_x based catalysts [12, 13] were shown to be efficient for catalytic destruction of chloroaromatics from industrial exhausts, though both are hazardous materials themselves. Inspired by the Deacon Reaction technology ($4HCl + O_2 \rightarrow 2Cl_2 + 2H_2O$) [14], Dai *et al.* have synthesized a RuO_x-TiO_2-CeO_2 catalyst capable of converting surface-bound Cl to Cl_2 [15]. However, Ru is costly and the activation barrier of Cl recombination on RuO_x has been calculated to be 228 kJ/mol [16], which renders the catalyst inactive at low temperatures. In particular, these catalysts all produce polychlorinated congeners, including dioxin-like by-products [10, 17, 18]. In addition to direct catalytic oxidation, a hydrolysis route has been considered to be promising for chlorinated organics elimination [19, 20]. This process is efficient at dechlorinating hydrocarbons and removing chlorine from the catalyst surface, but low-temperature catalysts have not yet been reported.

The Gulf Research & Development Company published a patent in 1973 that states rare earth (RE) metal phosphates can hydrolytically dechlorinate aryl halides into the corresponding ring-hydroxylated aryl compounds and HCl [4]. Weckhuysen and co-workers subsequently reported RE oxides, including La_2O_3, Pr_2O_3, Nd_2O_3 and CeO_2, were active in the hydrolytic destruction of CCl_4 [21-25]. However, based on theoretical investigations [21], the energy required for the dissociative adsorption of CCl_4 on the most active La_2O_3 was about 192 kJ/mol and that for the hydrolytic regeneration was about

180 kJ/mol. Such high energy barriers render the RE catalysts inactive below 300 °C, so are not intrinsically active enough to be of commercial interest.

In our previous work, we showed that phosphoric acid treatment is an effective way to etch and modify lanthanide oxides, which provided hydrolytic reactivity in the catalyst [26]. Dai *et al.* recently modified CeO_2 nanosheets using an organophosphate precursor, but did not describe any hydrolysis function in this catalyst [27, 28]. Herein we explored that phosphoric acid modified CeO_2 nanorods are highly active and stable catalysts for the hydrolytic destruction of chlorobenzene, a model chlorinated organic molecule. Subsequent density functional theory (DFT) calculations and catalyst characterization revealed the origin of the observed activity and a reaction pathway was proposed.

2. EXPERIMENTAL SECTION

2.1 Catalyst Synthesis

CeO_2 nanorods were synthesized according to previous work [29-31]. The process was as follows: $Ce(NO)_3 \cdot 6H_2O$ (1.736 g) and NaOH (19.2 g) were dissolved in 10 and 70 mL of deionized water, respectively. The two solutions were then combined and continuously stirred for 30 min. Then the mixed solution was transferred to a Teflon-lined stainless steel autoclave and hydrothermally treated at 100 °C for 24 h to form the CeO_2 nanorods. The formed solids were recovered by centrifugation and washed with deionized water and ethanol several times, followed by drying at 100 °C for 8 h.

Phosphate-functionalized CeO_2 (hereafter denoted as HP-CeO_2) was prepared using a wet impregnation method. CeO_2 nanorods were initially washed with ethanol to introduce surface hydroxyl groups [32], and enhance the anchoring of phosphate groups on the CeO_2 surface. CeO_2 nanorods (1.0 g) and an aqueous solution of H_3PO_4 (0.1 M, 25 mL) were mixed at 25 °C and stirred for 1 h. The mixture was then washed with deionized water (2 L) several times until the pH reached *ca.* 7, followed by drying at 100 °C overnight.

2.2 Catalytic activity and by-product analyses

Catalytic activity was measured in a fixed-bed reactor, in which 1.0 g of catalyst was loaded into an 8 mm reactor tube and secured in place between plugs of silica wool. The reaction feed consisted of 500 or 200 ppm chlorobenzene, 145 mL/min N_2, 15

mL/min O_2 with a gas hourly space velocity (GHSV) at 10000 h^{-1}. The reaction temperature was controlled using a thermocouple placed in the center of the catalyst bed. Catalysts were evaluated over the range 150-250 °C. All catalysts were sieved to 40-60 mesh and pre-treated at 300 °C for 1 h in the flow of He before each measurement. The concentration of chlorobenzene, along with CO_2 and CO production, were analyzed on–line using a gas chromatograph (GC, Agilent 6890, America) equipped with a flame ionization detector (FID) preceded by a methanizer, and an electron capture detector (ECD). Experiments with 0.5 vol.% H_2O (CB/H_2O = 1/10) were carried out by feeding a N_2 flow (15 mL/min) through a water saturator at a fixed temperature to achieve a partial pressure of approximately 0.5 vol.%. The water container was kept at 30 °C and the transfer line was set as short as possible so as to prevent condensation.

The concentration of Cl^- from HCl was measured using an ion chromatograph instrument (Shimadzu LC-20A, Japan) equipped with a Shim-pack IC-A3 adsorption column. In a lab-scale measurement, the establishment of Cl balance during the catalytic oxidation of chloroaromatics is very difficult. The generated HCl preferentially adsorbs on the stainless steel lines of the reactor and leads to very few HCl in the effluent gases. As such, measurements on the HCl production usually require an enrichment process where a 0.0125 mol/L NaOH solution was used to adsorb the HCl for a defined time period of 30 min. The quantitative measurements (even ignoring the error) could only reveal the trend in HCl production for each catalyst.

The quantitative identification of gaseous by-products was achieved with a calibrated GC/MS system. The gaseous by-products were sampled from the off-gases in a gas sampling bag (Teflon®FEP, 1 L volume). The sample was the injected by an autosampler (ENTECH 7016), and pre-concentrated according to the EPA method TO-15 (US EPA, 1999) using a pre-concentrator (ENTECH 7200). After the sample gas (400 mL) was pre-concentrated on the trap, the trap was heated and the VOCs were thermally desorbed and refocused on a cold trap. This trap was further heated and the VOCs were thermally desorbed again onto the head of the capillary column. Then, the oven temperature (programmed) increased and the VOCs began to elute and were analyzed by the GC/MS system (Agilent 6890N GC equipped with Agilent 5977B MS) with a DB-624 (60 m × 0.25 mm × 1.4 μm, 6% cyanopropyl-phenyl / 94%

dimethylpolysiloxane, Agilent Technologies, USA) capillary column. The GC oven temperature was initially held at 35 °C for 3 min, then increased to 140 °C at the rate of 6 °C/min, finally increased to 220 °C at the rate of 10 °C/min and held at 220 °C for 3 min (whereas held at 220 °C for 2 min for post-operation). The mass spectrometer was operated in the electron impact ionization mode using selected ion monitoring (SIM). The ion source temperature was set at 230 °C.

The surficial semi-volatiles organic residual on the catalyst surface were extracted using dichloromethane, where 5 mL dichloromethane and 1 g catalyst were mixed in a glass bottle and ultrasonically oscillated in an ice-bath for 30 min. The above process (mixing, oscillation and extraction) was repeated once. The extracted liquid was then transferred into a test-tube and concentrated to 0.5 mL using a nitrogen blower. The liquid was filtered and eventually 0.5 μL of the filtrate were splitless injected into a GC/MS system (the same as used in the qualitative identification) for analyses.

In dioxin measurements, the off-gas from CB oxidation was collected by absorption in a 100 mL toluene for 10 h. The total extract was then concentrated to about 1 mL by rotary evaporation and exchanged by 10 mL hexane for further pre-treatment. Both pre-treatment and determination of PCDD/F were conducted according to EPA method 1613 (US EPA, 1994). Sample clean-up involved percolation through a multi-silica gel column and a basic-alumina column. Then, the eluate again was concentrated, while being blown by nitrogen to approximately 20 μL. Finally, the cleaned solution was spiked with known amounts of a Method 1613 standard solution. The recovery efficiency of each internal standard was established at between 60% and 115%, conforming to the required 40–130%. All analyses were performed by HRGC/HRMS on a 6890 Series gas chromatograph (Agilent, USA) and coupled to a JMS-800D mass spectrometer (JEOL, Japan). A DB-5MS (60 m × 0.25 mm I.D., 0.25m film thickness) capillary column was used for separation of the PCDD/F congeners. The GC temperature program was optimized as follows: splitless injection of 2 μL at 150 °C, initial oven temperature of 150 °C for 1 min, then increased at 25 °C/min to 190 °C, finally increased at 3 °C/min to 280 °C and held for 20 min. Helium was used as the carrier gas. The mass spectrometer was operated in the electron impact ionization mode using selected ion monitoring (SIM). Electron energy was set to 38 eV. Source temperature was 280 °C. The mass system was tuned to a minimum resolution of 10,000

(10% valley) using perfluorokerosene (PFK) as lock mass. The detailed quantitative determination of PCDD/Fs was referred to US EPA method 1613.

2.3 Catalyst Characterization

P loading was analyzed using a Perkin Elmer Optima 2100 DV Inductively Coupled Plasma Optical Emission Spectrometer (ICP-OES). The sample (*ca.* 10 mg) was digested in 5 mL of 4 M HCl, 1 mL concentrated HNO_3, and 2 mL of 30 v/v% H_2O_2, then sonicated for ten minutes, and placed into a 50 °C water bath for 12 h. Thereafter, the sample was diluted to 10 mL of total solution.

Transmission electron microscopy (TEM) was carried out to monitor the structural changes of CeO_2 using a FEI TECNAI G2 20 XTwin HRTEM working at an accelerating voltage of 200 kV. The samples for TEM measurements were drop-casted onto carbon coated copper grids from an ethanol suspension.

In situ FTIR was conducted by using a Nicolet 6700 FTIR spectrometer equipped with a MCT detector. The FTIR cell (Harrick) had CaF_2 windows allowing the catalyst to be heated to 400 °C at atmospheric pressure. In each measurement, the catalyst was pretreated in a flow of He (99.99%, 30 mL/min) at the temperature of 350 °C for 1 h and then allowed to cool to room temperature. The background spectrum, recorded under flowing He, was subtracted from the sample spectrum. For H_2O adsorption measurements, the H_2O was introduced by saturating the N_2 carrier gas through a Dreschel Bottle containing deionized H_2O (N_2 was pre-dehydrated using molecular sieve). For FTIR studies of CB oxidation, 200 ppm of CB, O_2 (10 vol.%), 2000 ppm H_2O (injected using a micro injection pump) and the N_2 carrier gas were introduced at 150 °C for 30 min. In NH_3-IR, the N_2 carrier gas with 5 vol.% NH_3 was purged through the catalyst at 150 °C for 30 min. The spectra (average of 64 scans at 4 cm^{-1} resolution) were simultaneously recorded at different times in each run. The final differential sample spectra were calculated by applying the Kubelka–Munk function.

X-ray photoelectron spectroscopy (XPS) was performed on a Kratos Axis Ultra-DLD photoelectron spectrometer, using monochromatic Al Kα radiation at 144 W (12 mA × 12 kV) power. High resolution and survey scans were performed at pass energies of 40 and 160 eV respectively. Magnetically confined charge compensation was used to minimize sample charging and the resulting spectra were calibrated to the C(1s) line at 284.8 eV.

Powder X-ray diffraction (XRD) patterns were recorded using a Riga ku D/max-2500 powder diffractometer with Cu Kα radiation source (operated at 40 kV and 40 mA, wavelength 0.15418 nm), the data were collected over the 2θ range from 10° to 80°.

O_2 temperature programmed desorption (O_2-TPD) was carried out on a custom-built apparatus (TP-5089, Tianjin Xianquan Co., Ltd., China), connected to a mass spectrometer (HIDEN QGA, UK). 100 mg of catalyst was first pretreated in a 5 % O_2/He gas flow at 350 °C for 1 h and then cooled to room temperature. After purging pure He for 1 h, the catalyst was heated to 800 °C at the rate of 10 °C/min. The signals of desorbed O_2 was recorded using a MS.

NH_3 temperature programmed desorption (NH_3-TPD) was carried out on a custom-built apparatus (TP-5089, Tianjin Xianquan Co., Ltd., China), connected to a mass spectrometer (HIDEN QGA, UK). 100 mg of catalyst was first pretreated in a He gas flow at 350 °C for 1 h and then cooled to room temperature. Afterwards, a flow of 6 % NH_3/He was introduced for 30 min. Then the gas flow was switched back to pure He for 30 min. The catalyst was reheated to 600 °C at the rate of 10 °C/min. The signals of desorbed NH_3 was recorded using a MS.

2.4 DFT calculations

All the first-principles calculations were based on Hubbard-corrected density-functional theory (DFT+U) with U = 5.0 eV for Ce using the Vienna *ab initio* simulation package (VASP). The Perdew-Burke-Ernzerhof generalized gradient approximation (PBE-GGA) exchange-correlation potential was used, and ionic potentials were treated by the projector-augmented wave (PAW) pseudopotential method. The kinetic energy cutoff was set to 400 eV. The Brillouin zone integration was performed with a single gamma point for geometric optimization. The convergence criteria for the electronic energy and the geometry relaxation were set to 10^{-4} eV and 0.03 eV/Å, respectively. A vacuum layer of at least 15 Å thick was added in the slab cell along the direction perpendicular to the surface in order to avoid the artificial interactions between the model and its periodic images. The CeO_2(110) surface was modeled with a supercell (4×3) approach by periodically repeated slabs. Optimized model of CeO_2 were constructed by removing single oxygen atom from CeO_2 supercell to introduce oxygen vacancies (**Figure S1**). During geometry optimization, the atoms

in the top two layers of CeO_2 slab were allowed to relax while atoms in the bottom two layers were fixed in their optimized bulk positions. The model of HP-CeO_2 was constructed by a phosphate group adsorbed on the CeO_2 surface (indicated as H_2PO_4/CeO_2), with corresponding molecule adsorbed on the phosphate group. During geometry optimization, the atoms in the two layers of CeO_2 slab were fixed in their optimized surface positions.

The adsorption energy (E_{ad}) of molecular adsorbates on the substrate was calculated as:

$$E_{ad} = E_{sub} + E_{mol} - E_{tot}$$

where E_{sub}, E_{mol} and E_{tot} are the total energies of optimized clean substrates, molecular adsorbates in the gas phase and substrates with molecular adsorbates, respectively.

The formation energy of an oxygen vacancy (E_v) was calculated by:

$$E_v = E_{vac} + \frac{1}{2}E_{O2} - E_{tot}$$

where E_{vac} and E_{tot} are the total energies of the model with and without an oxygen vacancy on the CeO_2 surface. And E_{O2} is the total energy of an oxygen molecule in the gas phase. A positive value for E_v means that energy is needed to create an oxygen vacancy.

3. RESULTS AND DISCUSSIONS

3.1 Phase Identification

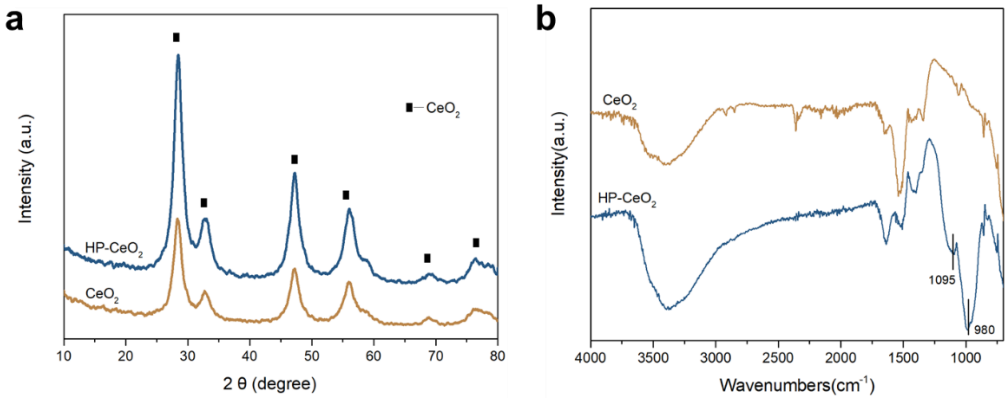

Figure 1. (a) X-ray powder diffraction patterns and **(b)** IR spectra of CeO_2 and HP-CeO_2 catalysts

As identified by XRD analyses (**Figure 1**), both CeO_2 and HP-CeO_2 catalysts could be indexed to the face-centered cubic fluorite structure with space group Fm-3m (JCPDS 34-0394), and no evidence of phosphate-related structures and bulk $CePO_4$ was

observed. According to ICP-OES results, the loading of P in the HP-CeO_2 was measured at approximately 6.64 $g/kg_{catalyst}$ (0.6 wt%). This corresponds to approximately 1.18 P-atoms per nm^2 of catalyst and essentially represents a surface unsaturation as the theoretical quantity of Ce atoms on preferentially exposed (110) surface in CeO_2 nanorod [30, 33] is approximately 19.4 Ce-atoms per nm^2 [34]. Obviously, bulk phosphate (M_xPO_4) would be not generated in the HP-CeO_2 as it only forms under sufficiently high P loading [32]. TEM (**Figure S2**) and surface area analyses (**Table S1**) suggested the modification with H_3PO_4 did not distinctly change the crystal morphology and surface area of CeO_2 nanorods.

To confirm the successful anchoring of phosphate groups, FTIR was carried out and the spectra are shown in **Figure 1(b)**. In comparison with CeO_2, HP-CeO_2 exhibited two additional bands. The bands located at 980 and 1095 cm^{-1} were assigned to symmetric stretching ν_s(P-O) and asymmetric stretching ν_{as}(P-O) of PO_4 entities, respectively [35, 36], confirming the immobilization of phosphate groups on the CeO_2 surface. No characteristic bands for P-O-P species (ν_s = 759-767 cm^{-1} and ν_{as} = 925-934 cm^{-1} [37]) were observed, which indicated that the phosphate species is present as an orthophosphate rather than a pyrophosphate. A broad band at 3000 - 3650 cm^{-1} was observed in the CeO_2 and HP-CeO_2. This could originate from the hydroxyl groups associated to Ce^{3+} sites [38] or the P-OH groups [32].

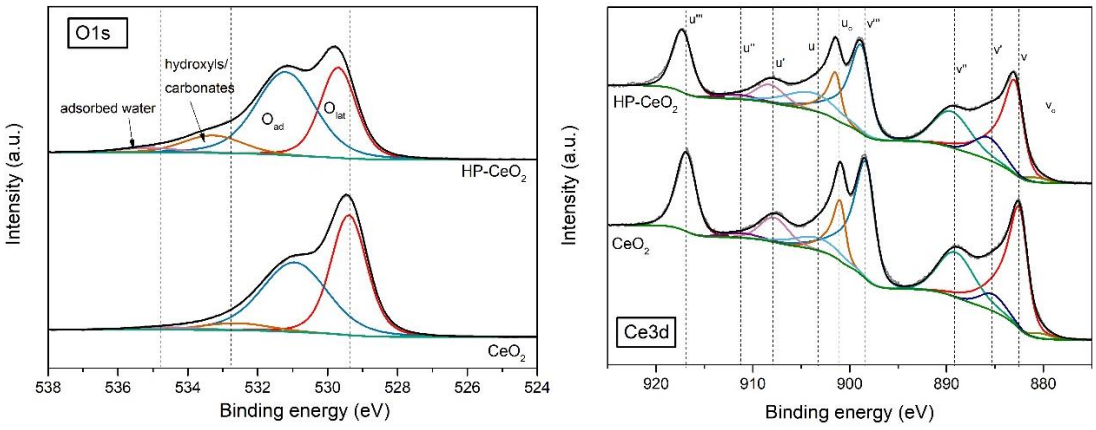

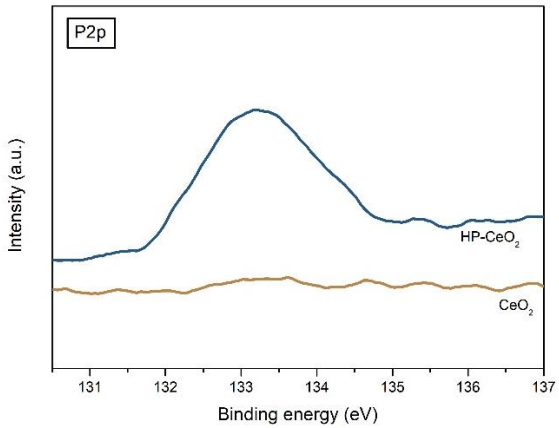

Figure 2. Ce3d, O1s and P2p XPS spectra of CeO_2 and HP-CeO_2 catalysts

The chemical nature and composition of surface species of CeO_2 and HP-CeO_2 were probed *via* XPS analyses (see **Figure 2**), which revealed CeO_2 with four O 1s XPS peaks centered at 529.7, 531.2, 533.3, 535.2 eV, corresponding to lattice oxygen of the ceria, oxygen defect sites, hydroxyl or carbonate groups and adsorbed molecular water, respectively [39, 40]. The Ce 3d spectrum revealed characteristic u_0, u', v_0, v' signals for Ce^{3+} and u''', u'', u, v''', v'', v peaks for Ce^{4+} [30]. It should be noted the presence of molecular water is, understandably, contentious given the samples are analyzed under vacuum where the water would be expected to be lost. We believe a more plausible explanation for this signal is due to changes in the background and peak broadening due to a greater defect density as implied by the Ce(IV)/Ce(III) ratio in the Ce(3d) spectra (**Table S1**).

HP-CeO_2 exhibited similar oxygen species, but the concentration of each species was different. In particular, the O species at 533 eV was much more pronounced than in CeO_2. This species has previously been assigned to P-OH and M-O-P species [41] and indicates the presence of phosphates at the surface. Additionally, the oxygen vacancy species at 531 eV was also more prominent in HP-CeO_2, especially when compared to the Ce-O lattice species at 529 eV. This suggested that the presence of phosphate groups on the surface promotes oxygen vacancy formation, although M-OH species are also found in this region. The P 2p XPS spectrum only revealed one peak, centered around 133.2 eV, further confirming phosphate species is present on the catalyst surface.

3.2 Redox and acidic properties analyses

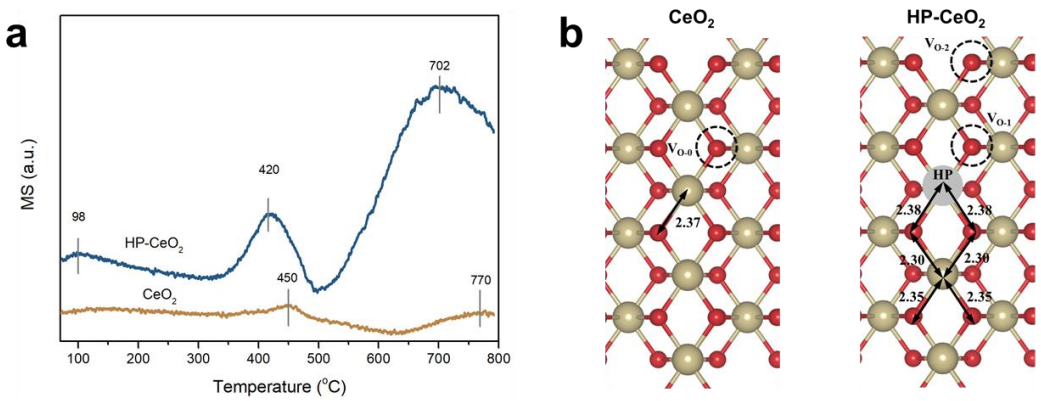

Figure 3. (a) O_2-TPD, **(b)** DFT calculations profiles of CeO_2 and HP-CeO_2 catalysts. Atoms with red and yellow colors represent oxygen and cerium atoms, respectively.

To gain an insight into the redox properties of CeO_2 and HP-CeO_2, O_2-TPD was conducted. In general, the desorbed oxygen species can be categorized into chemisorbed oxygen species (α-O) at 100-300 °C, superficial lattice oxygen (α'-O, including the nonstoichiometric oxygen α''-O) at 300-600 °C and bulk lattice oxygen (β-O) above 600 °C [26]. As depicted in **Figure 3(a)**, CeO_2 exhibited two main desorption peaks with maxima at 450 °C and 770 °C. The former peak was assigned to the superficial lattice oxygen generated from grain boundaries and dislocations, and the latter was related to the bulk oxygen desorbed *via* vacancy migration inwards with the increase of temperature [30, 39]. For HP-CeO_2, the oxygen desorption peaks both strengthened and shifted to a lower tempeature range, and a new peak located at 98 °C appeared, which corresponded to oxygen chemisorbed on the surface of oxygen vacancies (α-O) [42]. In comparison with CeO_2, HP-CeO_2 exhibited enriched α'-O and β-O species and extra α-O species, revealing an enhanced oxidation ability by acid modification.

In order to elucidate the cause for such an enhancement, DFT calulations were carried out. According to DFT calculations (**Figure. 3(b)**), after the deposition of the phosphate, the formation energy of a CeO_2 oxygen vacancy at nearest (V_{O-1}) and next-nearest (V_{O-2}) sites to the phosphate groups was only 0.46 eV and 0.77 eV, respectively, whereas for stoichiometric CeO_2, this energy was 2.11 eV. This result is consistent with the XPS O1s analyses (**Figure. 2(a)**), and explained why the HP-CeO_2 exhibited labile active oxygen species in the catalyst.

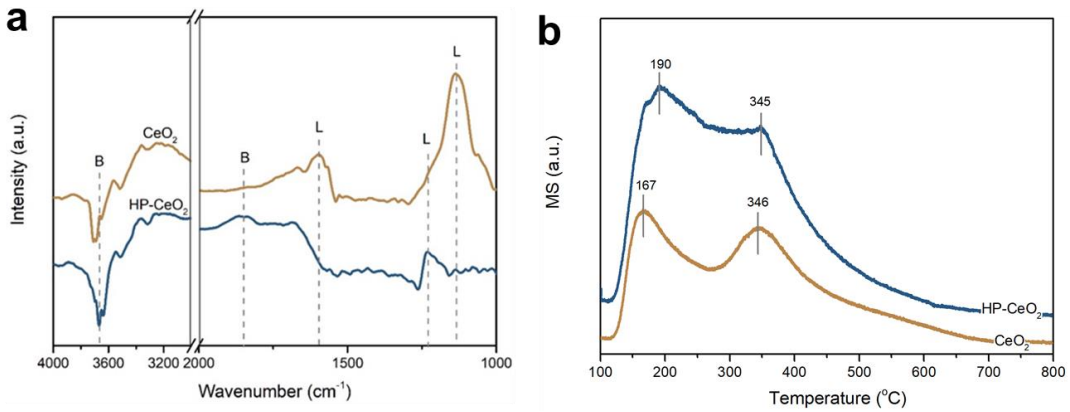

Figure 4. **(a)** NH_3-IR and **(b)** NH_3-TPD profiles of CeO_2 and HP-CeO_2 catalysts

The acidic properties of CeO_2 and HP-CeO_2 were evaluated using NH_3-IR and NH_3-TPD. As shown in **Figure 4(a)**, for the CeO_2, an intense band at 1135 cm^{-1} and a weaker one at 1595 cm^{-1} were observed. Both bands were assigned to adsorbed NH_3 on Lewis acid sites [43]. The negative band located at 3680 cm^{-1} could be assigned to the OH stretch of Brønsted acid sites due to the interaction of surface hydroxyls with NH_3 [44, 45]. HP-CeO_2 exhibited two additional bands at 1235 cm^{-1} and 1850 cm^{-1}, while the features at 1135 and 1595 cm^{-1} disappeared. The band at 1235 cm^{-1} was related to Lewis acid sites while 1850 cm^{-1} was associated with Brønsted acid sites [43]. The negative band at 3680 cm^{-1} was more intense in HP-CeO_2 than that in the CeO_2. These data suggested that acid modification resulted in an enhancement of Brønsted acid sites at the expense of Lewis acid sites. The concentration of acid sites was measured using NH_3-TPD. As shown in **Figure 4(b)**, HP-CeO_2 exhibited two more intense NH_3 desorption peaks at 190 ^oC and 345 ^oC, which corresponded to weak acid sites that originated from the desorption of NH_3 adsorbed on $Ce^{4+/3+}$ and surface acidic hydroxyl groups (mainly originted from phosphate groups) [27]. The acid site density of CeO_2 was measued at 0.205 mmol/g, which was two-fold lower than that of HP- CeO_2 (0.523 mmol/g).

3.3 Catalytic activity measurements

Figure 5 (a) illustrated the stability tests of CB catalytic oxidation over CeO_2 and HP-CeO_2 catalysts under the dry and humid conditions. It was noted that, in dry conditions, both HP-CeO_2 and CeO_2 were initially active but rapidly deactivated at 250 °C; the CB conversion rate both decreased to less than 30% after 200 min. In comparison, the introduction of excessive H_2O vapor (CB/H_2O = 1/10) yielded a stable CB conversion for HP-CeO_2. Approximately 90% CO_2 selectivity was obtained in the catalyst. Such a high stability was confirmed by lowering the conversion to

approximately 40% (by dropping the reaction temperature to 230 °C). At this temperature, the conversion of CB was unchanged after 40 h on-stream (**Figure. S3**). **Figure 5(b)** illustrated the HCl production in the off-gas at different temperatures. Although a full Cl balance was not possible to calculate due to the high affinity of HCl for the inside of the stainless steel reactor, the HCl production over HP-CeO_2 was nearly ten-fold higher when water vapor was present; this was also the case at reaction temperatures of 150 and 200 °C. These findings strongly suggested that the presence of water facilitates chlorine desorption (as HCl), thus greatly enhancing the stability by replenishing active sites. The accumulation of chlorine on the catalyst surface after reaction was also measured using ion chromatography. It was noted that under the dry condition, 8.25 $g/kg_{catalyst}$ and 10.36 $g/kg_{catalyst}$ for HP-CeO_2 and CeO_2, respectively, of chlorine was present in the post-reaction samples, while in the presence of water vapor, the residual 7.56 $g/kg_{catalyst}$ of chlorine was measured for CeO_2, but only 2.36 $g/kg_{catalyst}$ for HP-CeO_2. Additionally, the content of P after stability measurement at 250 °C was also measured, and the results showed the P content was decreased by 5.9%, suggesting that significant P were retained after tests.

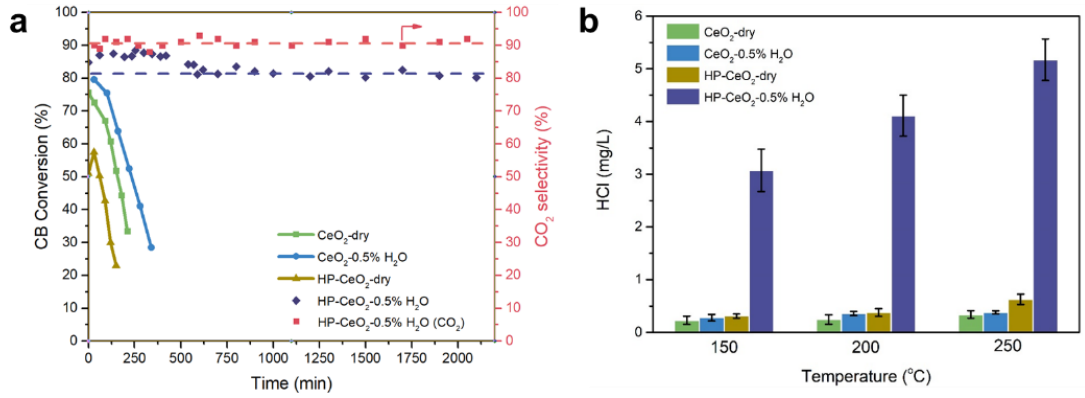

Figure 5. **(a)** Stability measurements of CeO_2 and HP-CeO_2 catalysts with and without water vapor at 250 °C; **(b)** HCl productions of CeO_2 and HP-CeO_2 catalysts with and without water vapor at 250 °C. Reaction conditions: GHSV = 10,000 mL/(g h), 500 ppm chlorobenzene, 0.5 % H_2O, N_2 flow rate = ca. 145 mL/min, O_2 flow rate = ca. 15 mL/min.

3.4 *in-situ* FT-IR analyses

To gain an insight into the reaction mechanism, *in-situ* FTIR analyses were conducted. **Figure 6(a)** showed the spectra collected at 150 °C under the dry stream of CB and O_2 over HP-CeO_2. The bands at 1585 and 1478 cm^{-1} are assigned to the C=C degenerate stretching vibrations of the aromatic ring [46]. The bands at 2000-1700 cm^{-1}

were associated with harmonics (combinations and overtones) of out-of-plane C-H deformation modes [47], with side-on adsorption geometry, and originate from the π-type aromatic clouds on electron-withdrawing centers of the metal oxides [48]. It was noted that these characteristic bands for CB adsorption increased in the first 10 min and then gradually decreased. In general, CB adsorption on the CeO_2 surface could be through a π-complex between surface Ce^{4+} and aromatic ring [49]. Such a complex is formed both on dehydroxylated and fully hydroxylated surface via either the $Ce^{4+}\cdots\pi$-electron interaction or dual-site interaction (OH···π-electron and OH···Cl). In this work, since the CeO_2 nanorods were washed by ethanol, initially, the abundant surface hydroxyls would provide sufficient sites for dual-site CB adsorption, resulting in the formation of phenolate species. Over time, these hydroxyls were gradually consumed and the phenolates were oxidized. A broad band centered at 1650 cm^{-1} started to grow and dominated after 30 min. This band was assigned to vibrations of CB adsorbed on the surface oxygen vacancies [50], indicating that CB adsorption on the oxygen vacancies began to dominate the process after the hydroxyls had been fully consumed. The CeO_2 catalyst revealed similar FTIR spectra to HP-CeO_2 (**Figure S4**), suggesting that without H_2O, the adsorption of CB on these two catalysts were analogous, which is consistent with their activity measurements (**Figure 5**).

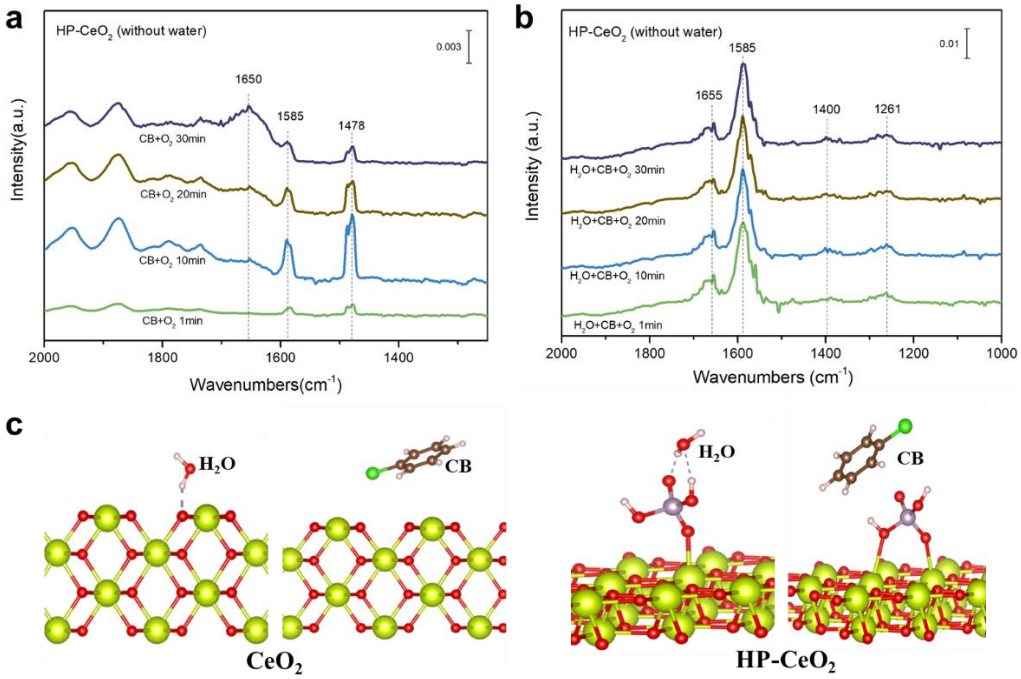

Figure 6. *in-situ* FTIR spectra of CB oxidation over HP-CeO_2 at 150 °C **(a)** without or **(b)** with H_2O; **(c)** optimized models of adsorbed H_2O and C_6H_5Cl molecule at CeO_2 and HP-CeO_2 surfaces.

Figure 6(b) illustrates the spectra collected from CB oxidation with the addition of water vapour. It was noted that the peak located at 1585 cm^{-1} dominated the spectra, suggesting that the CB was only adsorbed via the π-type interaction with surface hydroxyl groups. Furthermore, the harmonics in the range of 2000-1700 cm^{-1} were not observed, which indicated that in the presence of H_2O, the CB did not adsorb on the surface oxygen vacancies. According to DFT calculations (**Figure 6(c)** and **Table S2**), the co-adsorption energy of CB and O_2 on an oxygen vacancy (O_{vac}) of CeO_2 nanorods was 2.37 eV. This indicated that the CB would preferentially adsorb on an O_{vac} in the presence of O_2, which then dissociate to leave Cl, inhibiting further activation of O_2 and leading to catalyst deactivation. After acid modification and in the presence of H_2O, CB was found to preferentially co-adsorb with H_2O on the phosphate groups with a calculated co-adsorption energy of 2.77 eV. This was even larger than the sum of the individual adsorption energies of CB (0.5 eV) and H_2O (0.63 eV) and suggested that on the HP-CeO_2 catalyst with H_2O present, CB adsorption mainly occurs on the phosphate group rather than on the O_{vac}. Such a co-adsorption was shown to induce a hydrolysis reaction and converted the CB into phenol (band at 1585 cm^{-1} in **Figure 6(b)**) and HCl (**Figure 5(b)**), leading to excellent stability in the hydrolytic destruction of CB.

3.5 By-products analyses

Any residual compounds on the catalyst were extracted using dichloromethane, and then injected into GC/MS system for analyses. As shown in **Figure 7(a)**, after the 250 ^oC with H_2O, HP-CeO_2 did not retain chlorinated organics on the surface. Only trace amounts of alcohols and phenol species were detected, further suggesting the occurrence of hydrolysis reaction on the catalyst. As for the CeO_2, distinct dichlorobenzene was detected, which could be converted into chlorophenol and subsequently condense to form the PCDD/Fs [51].

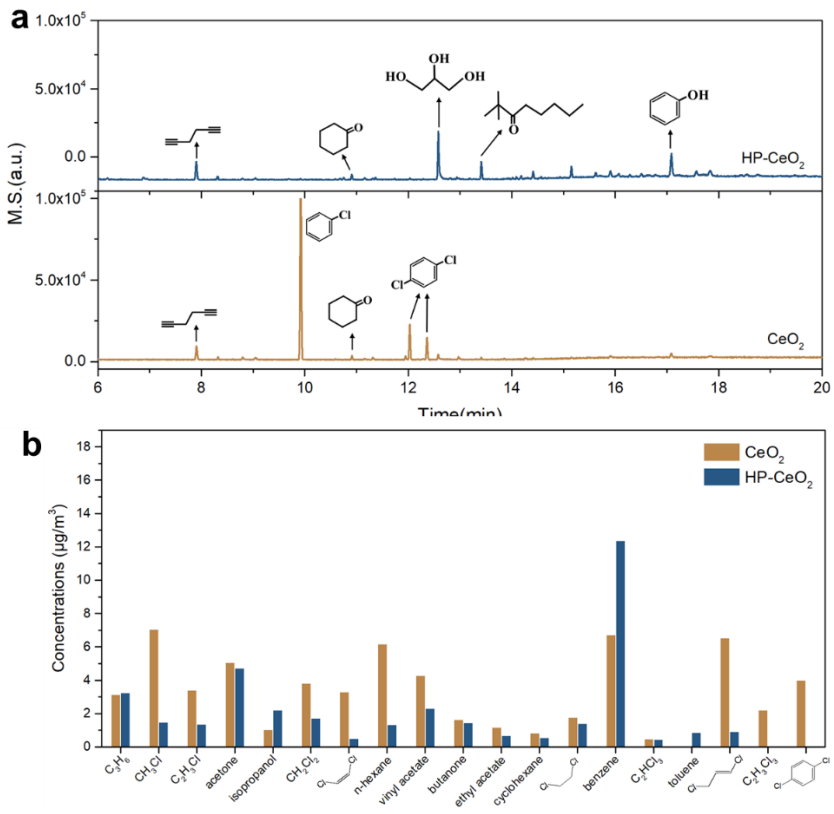

435

436 **Figure 7. (a)** Coke accumulation on the catalyst surface and **(b)** gaseous compounds in the effluent
437 in the catalytic oxidation of CB over HP-CeO_2 and CeO_2 in the presence of H_2O stream (Note: other
438 tiny peaks unlabeled present for Si-O analogous came from the chromatographic column or long-
439 chain organics).

440 The organic by-products in the off-gas were quantitatively identified. This was
441 conducted through capturing the off-gas in an airbag, and analyzed using a calibrated
442 GC/MS system. As shown in **Figure 7(b)**, approximately 19 types of organic products
443 were detected in the off-gas. The HP-CeO_2 at 250 ^oC test with H_2O exhibited fewer
444 chlorinated organics (less than 8 $\mu g/m^3$) in comparison with the CeO_2 (about 30 $\mu g/m^3$).
445 In particular, this catalyst did not generate dichlorobenzene in the off-gas where the
446 CeO_2 produced 4.11 $\mu g/m^3$ *p*-dichlorobenzene, which would be transferred to
447 chlorophenols, leading to the condensation reaction forming dioxins. Indeed, after
448 being subjected to 17 toxic dioxins measurement (see **Table S3**), the CeO_2 generated
449 about 12 kinds of dioxin species in the off-gas (note: the surficial accumulation of
450 dioxin was negligible), but none of the dioxins were detected in the HP-CeO_2.

451

ASSOCIATED CONTENT

Supporting Information

TEM images, catalysis physical properties, stability test, additional FTIR analyses, DFT calculations and dioxin measurements are in the supplemental section. This material is available free of charge via the Internet at http://pubs.acs.org.

ACKNOWLEDGEMENT

This work was financially supported by the National Natural Science Foundation of China (Grant No. 21777140, 21922607) and the Outstanding Youth Project of Zhejiang Natural Science Foundation (Grant No. LR19E080004).

REFERENCES

1. Bumb, R. R.; Crummett, W. B.; Cutie, S. S.; Gledhill, J. R.; Hummel, R. H.; Kagel, R. O.; Lamparski, L. L.; Luoma, E. V.; Miller, D. L.; Nestrick, T. J.; Shadoff, L. A.; Stehl, R. H.; Woods, J. S., Trace chemistries of fire - a source of chlorinated dioxins. *Science* **1980,** *210* (4468), 385-390.

2. Schmittinger, P., Chlorine: principles and industrial practice. (John Wiley & Sons, 2008).

3. Davy, C. W., Legislation with respect to dioxins in the workplace. *Environ. Int.* **2004,** *30* (2), 219-233.

4. Procaccini, C.; Bozzelli, J. W.; Longwell, J. P.; Sarofim, A. F.; Smith, K. A., Formation of chlorinated aromatics by reactions of Cl·, Cl_2 and HCl with benzene in the cool-down zone of a combustor. *Environ. Sci. Technol.* **2003,** *37* (8), 1684-1689.

5. Liu, J. M. J., Agent-based dynamic component management. *Object-Oriented Technology* **1998**, 125-130.

6. Ren, Z. Y.; Lu, Y.; Li, Q. S.; Sun, Y. Z.; Wu, C. M.; Ding, Q., Occurrence and characteristics of PCDD/Fs formed from chlorobenzenes production in China. *Chemosphere* **2018,** *205*, 267-274.

7. Mosallanejad, S.; Dlugogorski, B. Z.; Kennedy, E. M.; Stockenhuber, M.; Lomnicki, S. M.; Assaf, N. W.; Altarawneh, M., Formation of PCDD/Fs in oxidation

of 2-chlorophenol on neat silica surface. *Environ. Sci. Technol.* **2016,** *50* (3), 1412-1418.

8. Du, C.; Lu, S.; Wang, Q.; Buekens, A. G.; Ni, M.; Debecker, D. P., A review on catalytic oxidation of chloroaromatics from flue gas. *Chem. Eng. J.* **2018,** *334*, 519-544.

9. De Jong, V.; Cieplik, M. K.; Louw, R., Formation of dioxins in the catalytic combustion of chlorobenzene and a micropollutant-like mixture on Pt/γ-Al_2O_3. *Environ. Sci. Technol.* **2004,** *38* (19), 5217-5223.

10. Liu, X.; Chen, L.; Zhu, T.; Ning, R., Catalytic oxidation of chlorobenzene over noble metals (Pd, Pt, Ru, Rh) and the distributions of polychlorinated by-products. *J. Hazard. Mater.* **2019,** *363*, 90-98.

11. Hutchings, G. J.; Heneghan, C. S.; Hudson, I. D.; Taylor, S. H., Uranium-oxide-based catalysts for the destruction of volatile chloro-organic compounds. *Nature* **1996,** *384* (6607), 341-343.

12. Debecker, D. P.; Bertinchamps, F.; Blangenois, N.; Eloy, P.; Gaigneaux, E. M., On the impact of the choice of model VOC in the evaluation of V-based catalysts for the total oxidation of dioxins: Furan vs. chlorobenzene. *Appl. Catal. B - Environ.* **2007,** *74* (3), 223-232.

13. Lichtenberger, J.; Amiridis, M. D., Catalytic oxidation of chlorinated benzenes over V_2O_5/TiO_2 catalysts. *J. Catal.* **2004,** *223* (2), 296-308.

14. Iwanaga, K.; Seki, K.; Hibi, T.; Issoh, K.; Suzuta, T.; Nakada, M.; Mori, Y.; Abe, T., *The development of improved hydrogen chloride oxidation process*. 2004; Vol. 1, p 1-11.

15. Dai, Q.; Bai, S.; Wang, J.; Li, M.; Wang, X.; Lu, G., The effect of TiO_2 doping on catalytic performances of Ru/CeO_2 catalysts during catalytic combustion of chlorobenzene. *Appl. Catal. B - Environ.* **2013,** *142*, 222-233.

16. Over, H., Atomic-scale understanding of the HCl oxidation over RuO_2, a novel deacon process. *J. Phys. Chem. C* **2012,** *116* (12), 6779-6792.

17. Huang, H.; Dai, Q.; Wang, X., Morphology effect of Ru/CeO_2 catalysts for the catalytic combustion of chlorobenzene. *Appl. Catal. B - Environ* **2014,** *158-159*, 96-105.

18. Huang, H.; Gu, Y.; Zhao, J.; Wang, X., Catalytic combustion of chlorobenzene over VO_x/CeO_2 catalysts. *J. Catal.* **2015,** *326*, 54-68.

19. Takita, Y.; Ninomiya, M.; Matsuzaki, R.; Wakamatsu, H.; Nishiguchi, H.; Ishihara, T., Decomposition of chlorofluorocarbons over metal phosphate catalysts - Part I. Decomposition of CCl_2F_2 over metal phosphate catalysts. *Phys. Chem. Chem. Phys.* **1999,** *1* (9), 2367-2372.

20. Deng, X. Y.; Ma, Z.; Yue, Y. H.; Gao, Z., Catalytic hydrolysis of dichlorodifluoromethane over nanosized titania-supported titanyl sulfate. *J. Catal.* **2001,** *204* (1), 200-208.

21. Van der Avert, P.; Podkolzin, S. G.; Manoilova, O.; De Winne, H.; Weckhuysen, B. M., Low‐temperature destruction of carbon tetrachloride over lanthanide oxide‐based catalysts: from destructive adsorption to a catalytic reaction cycle. *Chem.-Eur. J.* **2004,** *10* (7), 1637-1646.

22. Weckhuysen, B. M.; Rosynek, M.; Lunsford, J. H., Destructive adsorption of carbon tetrachloride on lanthanum and cerium oxides. *Phys. Chem. Chem. Phys.* **1999,** *1* (13), 3157-3162.

23. Van der Avert, P.; Weckhuysen, B. M.; Schoonheydt R. A., Low‐temperature destruction of chlorinated hydrocarbons over lanthanide oxide based catalysts. *Angew. Chem. Int. Ed.* **2002,** *41* (24), 4730-4732.

24. Podkolzin, S. G.; Manoilova, O. V.; Weckhuysen, B. M., Relative activity of La_2O_3, LaOCl, and $LaCl_3$ in reaction with CCl_4 studied with infrared spectroscopy and density functional theory calculations. *J. Phys.Chem. B* **2005,** *109* (23), 11634-11642.

533 25. Van der Avert, P.; Weckhuysen, B. M., Low-temperature catalytic destruction of
534 CCl_4, $CHCl_3$ and CH_2Cl_2 over basic oxides. *Phys. Chem. Chem. Phys* **2004,** *6* (22),
535 5256-5262.
536 26. Weng, X.; Meng, Q.; Liu, J.; Jiang, W.; Pattisson, S.; Wu, Z., Catalytic oxidation
537 of chlorinated organics over lanthanide perovskites: effects of phosphoric acid etching
538 and water vapor on chlorine desorption behavior. *Environ. Sci. Technol.* **2019,** *53* (2),
539 884-893.
540 27. Dai, Q.; Zhang, Z.; Yan, J.; Wu, J.; Johnson, G.; Sun, W.; Wang, X.; Zhang, S.;
541 Zhan, W., Phosphate-functionalized CeO_2 nanosheets for efficient catalytic oxidation
542 of dichloromethane. *Environ. Sci. Technol.* **2018,** *52* (22), 13430-13437.
543 28. Dai, Q.; Wu, J.; Deng, W.; Hu, J.; Wu, Q.; Guo, L.; Sun, W.; Zhan, W.; Wang, X.,
544 Comparative studies of P/CeO_2 and Ru/CeO_2 catalysts for catalytic combustion of
545 dichloromethane: From effects of H_2O to distribution of chlorinated by-products. *Appl.*
546 *Catal. B - Environ.* **2019,** *249*, 9-18.
547 29. Zhou, K. B.; Wang, X.; Sun, X. M.; Peng, Q.; Li, Y. D., Enhanced catalytic activity
548 of ceria nanorods from well-defined reactive crystal planes. *J. Catal.* **2005,** *229* (1),
549 206-212.
550 30. Hu, Z.; Liu, X.; Meng, D.; Guo, Y.; Guo, Y.; Lu, G., Effect of ceria crystal plane
551 on the physicochemical and catalytic properties of Pd/Ceria for CO and Propane
552 oxidation. *ACS Catal.* **2016,** *6* (4), 2265-2279.
553 31. Mai, H. X.; Sun, L. D.; Zhang, Y. W.; Si, R.; Feng, W.; Zhang, H. P.; Liu, H. C.;
554 Yan, C. H., Shape-selective synthesis and oxygen storage behavior of ceria
555 nanopolyhedra, nanorods, and nanocubes. *J. Phys. Chem. B* **2005,** *109* (51), 24380-
556 24385.
557 32. Decanio, E. C.; Edwards, J. C.; Scalzo, T. R.; Storm, D. A.; Bruno, J. W., FT-IR
558 and solid-state NMR investigation of phosphorus promoted hydrotreating catalyst
559 precursors. *J. Catal.* **1991,** *132* (2), 498-511.

560 33. Yang, C. W.; Yu, X. J.; Heissler, S.; Nefedov, A.; Colussi, S.; Llorca, J.; Trovarelli,
561 A.; Wang, Y. M.; Woll, C., Surface faceting and reconstruction of ceria nanoparticles.
562 *Angew. Chem. Int. Edit* **2017,** *56* (1), 375-379.
563 34. Madier, Y.; Descorme, C.; Le Govic, A. M.; Duprez, D., Oxygen mobility in CeO_2
564 and $Ce_xZr_{(1-x)}O_2$ compounds: Study by CO transient oxidation and O-18/O-16 isotopic
565 exchange. *J. Phys. Chem. B* **1999,** *103* (50), 10999-11006.
566 35. Pusztai, P.; Simon, T.; Kukovecz, A.; Konya, Z., Structural stability test of
567 hexagonal $CePO_4$ nanowires synthesized at ambient temperature. *J. Mol. Struc.* **2013,**
568 *1044*, 94-98.
569 36. Romero-Sarria, F.; Dominguez, M. I.; Centeno, M. A.; Odriozola, J. A., CO
570 oxidation at low temperature on $Au/CePO_4$: Mechanistic aspects. *Appl. Catal. B-*
571 *Environ.* **2011,** *107* (3-4), 268-273.
572 37. Lu, M. W.; Wang, F.; Chen, K. R.; Dai, Y. Y.; Liao, Q. L.; Zhu, H. Z., The
573 crystallization and structure features of barium-iron phosphate glasses. *Spectrochim.*
574 *Acta a.* **2015,** *148*, 1-6.
575 38. Romero-Sarria, F.; Martinez, L. M.; Centeno, M. A.; Odriozola, J. A., Surface
576 dynamics of Au/CeO_2 catalysts during CO oxidation. *J. Phys. Chem. C* **2007,** *111* (39),
577 14469-14475.
578 39. Zhang, J.; Tan, D.; Meng, Q.; Weng, X.; Wu, Z., Structural modification of
579 $LaCoO_3$ perovskite for oxidation reactions: The synergistic effect of Ca^{2+} and Mg^{2+} co-
580 substitution on phase formation and catalytic performance. *Appl. Catal. B-Environ.*
581 **2015,** *172*, 18-26.
582 40. Kang, S.; Wang, M.; Zhu, N.; Wang, C.; Deng, H.; He, H., Significant
583 enhancement in water resistance of Pd/Al_2O_3 catalyst for benzene oxidation by Na
584 addition. *Chinese Chem. Lett.* **2019,** *30* (7), 1450-1454.
585 41. Garcia-Sancho, C.; Cecilia, J. A.; Merida-Robles, J. M.; Santamaria Gonzalez, J.;
586 Moreno-Tost, R.; Infantes-Molina, A.; Maireles-Torres, P., Effect of the treatment with

587 H_3PO_4 on the catalytic activity of Nb_2O_5 supported on Zr-doped mesoporous silica
588 catalyst. Case study: Glycerol dehydration. *Appl. Catal. B-Environ.* **2018,** *221*, 158-
589 168.
590 42. Meng, Q.; Wang, W.; Weng, X.; Liu, Y.; Wang, H.; Wu, Z., Active oxygen species
591 in $La_{n+1}Ni_nO_{3n+1}$ layered perovskites for catalytic oxidation of toluene and methane. *J.*
592 *Phys. Chem. C* **2016,** *120* (6), 3259-3266.
593 43. Zhang, L.; Wang, D.; Liu, Y.; Kamasamudram, K.; Li, J. H.; Epling, W., SO_2
594 poisoning impact on the NH_3-SCR reaction over a commercial Cu-SAPO-34 SCR
595 catalyst. *Appl. Catal. B - Environ.* **2014,** *156*, 371-377.
596 44. Shi, X.; Liu, F.; Xie, L.; Shan, W.; He, H., NH_3-SCR performance of fresh and
597 hydrothermally aged Fe-ZSM-5 in standard and fast selective catalytic reduction
598 reactions. *Environ. Sci. Technol.* **2013,** *47* (7), 3293-3298.
599 45. Zhao, S.-Y.; Wang, S.-P.; Zhao, Y.-J.; Ma, X.-B., An in situ infrared study of
600 dimethyl carbonate synthesis from carbon dioxide and methanol over well-shaped
601 CeO_2. *Chinese Chem. Lett.* **2017,** *28* (1), 65-69.
602 46. Lichtenberger, J.; Amiridis, M., Catalytic oxidation of chlorinated benzenes over
603 V_2O_5/TiO_2 catalysts. *J. Catal.* **2004,** *223* (2), 296-308.
604 47. Larrubia, M. A.; Busca, G., An FT-IR study of the conversion of 2-chloropropane,
605 *o*-dichlorobenzene and dibenzofuran on V_2O_5-MoO_3-TiO_2 SCR-DeNOx catalysts.
606 *Appl. Catal. B - Environ.* **2002,** *39* (4), 343-352.
607 48. Ramis, G.; Busca, G.; Lorenzelli, V., Determination of the geometry of adsorbed
608 unsaturated molecules through the analysis of the CH out-of-plane deformation modes.
609 *J Electron Spectrosc* **1993,** *64*, 297-305.
610 49. Nagao, M.; Suda, Y. J. L., Adsorption of benzene, toluene, and chlorobenzene on
611 titanium dioxide. *Langmuir* **1989,** *5* (1), 42-47.
612 50. Huang, H.; Gu, Y.; Zhao, J.; Wang, X., Catalytic combustion of chlorobenzene
613 over VO_x/CeO_2 catalysts. *J. Catal.* **2015,** *326*, 54-68.

614 51. Altarawneh, M.; Dlugogorski, B. Z.; Kennedy, E. M.; Mackie, J. C., Mechanisms
615 for formation, chlorination, dechlorination and destruction of polychlorinated dibenzo-
616 p-dioxins and dibenzofurans (PCDD/Fs). *Prog Energ Combust* **2009,** *35* (3), 245-274.
617